International Journal of Hydrogen Energy 70 (2024) 548–556

Contents lists available at ScienceDirect

International Journal of Hydrogen Energy

journal homepage: www.elsevier.com/locate/he

Optimized base metals electrodeposition on Ni perforated plate type electrodes for high-performance alkaline water electrolysis

Francesco Di Franco [a], Andrea Zaffora [a,*], Davide Pupillo [b], Barbara Seminara [a], Ragne Pärnamäe [c,d], Michele Tedesco [c,e], Monica Santamaria [a]

[a] Department of Engineering, University of Palermo, Viale delle Scienze, Ed. 6, 90128, Palermo, Italy
[b] Dipartimento di Scienza Applicata e Tecnologia, Politecnico di Torino, Corso Duca degli Abruzzi 24, 10129, Torino, Italy
[c] Wetsus, European Centre of Excellence for Sustainable Water Technology, Oostergoweg 9, 8911 MA, Leeuwarden, the Netherlands
[d] Environmental Technology, Wageningen University, Bornse Weilanden 9, P.O. Box 17, 6708 WG, Wageningen, the Netherlands
[e] TNO Sustainable Processes and Energy Systems, Lange Kleiweg 137, 2288 GJ, Rijswijk, the Netherlands

ARTICLE INFO

Handling Editor: Dr F Gallucci

Keywords:
Hydrogen evolution reaction
Base metals electrodeposition
Nickel perforated electrode
Water electrolysis

ABSTRACT

Hydrogen is considered as one of the key energy carrier for the forthcoming green transition because of its high energy content and harmless combustion products. Water electrolysis, powered by green electricity, is one of the most efficient and promising technologies for H_2 production. Cheap and earth abundant metals-based electrocatalysts for Hydrogen Evolution Reaction (HER) are needed to drive a green transition based on hydrogen produced by water electrolysis.

Perforated plate type Ni electrodes are prepared by a cost-effective electroforming process, designed to work for water electrolysis in alkaline environment in a flow-through configuration facilitating the release of bubbles produced by HER. The aim of this work is to synthesize a catalyst layer based on NiCuMo alloy produced by an electrodeposition process tailored to maximize electrocatalytic performances, increasing the electrochemical surface active area (more than 50 times) and its activity. HER is studied in aqueous 1 M KOH solution and an overpotential of only 95 mV is measured to reach 100 mA cm^{-2}, assessing a Tafel slope of 61 mV dec^{-1}. 100 h durability test is successfully carried out demonstrating the high chemical and mechanical stability of so-prepared electrodes for next generation alkaline electrolyzers.

1. Introduction

Hydrogen is considered one of the most crucial chemicals for the immediate future of global economy since it can be used as energy carrier, facilitating the decarbonization of modern society [1–3]. Thus, it is vital to adopt alternative processes for hydrogen production. Among these alternatives, water electrolysis receives much attention due to its ability to facilitate a rapid transition from a fossil fuel-based economy to a hydrogen-based one on a global scale. Moreover, when water electrolysis is powered by renewable electricity, it allows to transition towards a sustainable, renewable energy-driven economy [4–6].

Water electrolysis is a process carried out in an electrochemical cell and it foresees gaseous hydrogen production at the cathode (Hydrogen Evolution Reaction, HER) and gaseous oxygen production at the anode (Oxygen Evolution Reaction, OER) [7,8]. The minimum (thermodynamic) cell voltage to electrochemically split a water molecule is 1.23 V at room temperature, which means a change in Gibbs free energy (ΔG) of ~237 kJ mol^{-1}. Large-scale deployment of green water electrolysis can be achieved only by decreasing the costs of the process by, for example, using renewable energy or bringing down the cost of electrolyzers. Although today green hydrogen production is still more expensive than blue hydrogen production (i.e. H_2 produced using fossil fuels, with carbon capture and storage) [9], renewable energy costs continue to decrease. The high costs of electrolyzers are in part due to expensive platinum group metals (PGMs)-based electrodes used to catalyze HER and OER reactions with the lowest possible applied cell voltage. Alternatively, much cheaper non-noble electrocatalytic materials could be used instead. For alkaline water electrolysis, nickel-based HER electrocatalysts are the most used electrode materials [10–12]. However, Ni does not outperform PGM-based electrocatalysts. Thus, alloying Ni with other transition metals (TMs) is one of the approaches to enhance Ni activity for HER. Ni-Co [13], Ni-Mo [14–17] and NiCuMo [18–21] have

* Corresponding author.
E-mail address: andrea.zaffora@unipa.it (A. Zaffora).

https://doi.org/10.1016/j.ijhydene.2024.05.164
Received 29 February 2024; Received in revised form 26 April 2024; Accepted 10 May 2024
Available online 18 May 2024
0360-3199/© 2024 The Authors. Published by Elsevier Ltd on behalf of Hydrogen Energy Publications LLC. This is an open access article under the CC BY-NC-ND license (http://creativecommons.org/licenses/by-nc-nd/4.0/).

been shown in previous works as the most active and stable Ni-based electrocatalysts. An electrocatalytic material's performance can be further enhanced by increasing its electrochemical surface area (ECSA), i.e. the number of active sites available for the reaction. ECSA can be increased by optimizing the morphology of the electrocatalytic materials and by a proper selection of a metal substrate hosting the catalytic layer. The substrate must be mechanically and chemically stable, since alkaline water electrolyzers commonly operate at elevated pressures and temperatures, with electrodes submerged in corrosive alkaline electrolyte solution. Moreover, electrodes must be robust enough to withstand to the electrolyte flowing, which facilitates the release of gas bubbles whose accumulation otherwise causes large ohmic drop in the process [22–24], avoiding any possible detachment of catalyst layer with consequent degradation in performances during time.

Despite the active research field, the optimization of functionalized Ni-based electrodes for HER is still far from being optimized. In particular, a chemical formulation based on abundant and cost-effective metals is of outmost importance to reduce electrode costs and allow large-scale electrolyzer manufacturing [25].

In this work we exploited the possibility to use a nickel electrode with a tailored distribution of holes that can be easily prepared by Veco with the idea of optimizing in the follow up research activity to optimize their design to improve products degassing. The latter can be an issue especially with foam-type electrodes (depending on their thickness and on the micro-holes diameter). Notably, both foam and mesh need a surface functionalization to enhance their electrocatalytic activity. Therefore, we prepared electrodes for HER by depositing electrocatalytic material (a ternary coating containing Ni, Cu and Mo) on a perforated Ni plate substrate, using an optimized electrodeposition process to produce cost-effective, highly active and stable electrodes. Electrodes were characterized with Scanning Electron Microscopy (SEM) to study the morphology of the electrocatalytic coatings, and by Energy Dispersive X-ray (EDX) and X-Ray Photoelectron Spectroscopy (XPS) analysis to estimate the composition of the coatings. Electrochemical performances, i.e. activity toward HER, were studied in aqueous 1 M KOH solution by galvanodynamic measurements and EIS (Electrochemical Impedance Spectroscopy). The stability of the coating was assessed by galvanostatic measurements (0.1 A cm^{-2}) in a flow-through cell configuration for 100 h.

2. Materials and methods

2.1. Electrodeposition of electrocatalysts

Perforated Ni plate electrodes (thickness 300 μm, hole diameter 1 mm) were provided by Veco Precision BV (The Netherlands) and used as a substrate for the coatings. The electrodeposition has been carried out in a three-electrode cell with the perforated Ni plate substrate, a platinum mesh and silver/silver chloride electrode (SSC, E_{eq} = 200 mV SHE) being working, counter and reference electrode, respectively. Ni substrate was first ultrasonically cleaned in 5 M HCl aqueous solution (10 min treatment), then cleaned with milliQ water and, finally, dried in air. Electrodeposition bath consisted of an aqueous solution containing Ni-based (0.5 M $NiSO_4$) and Cu-based (12.5 mM $CuSO_4$) salts, boric acid (H_3BO_3, concentration: 0.5 M) with varying Mo-based salt ($(NH_4)_6Mo_7O_{24}$ concentration (i.e. 0.014 M, 0.028 M, 0.042 M or 0.056 M). Solution pH was brought to 2.5 by adding of H_2SO_4. Catalytic layer electrodeposition was performed with a VERSASTAT 3 potentiostat at electrode potential = −2 V Ag/AgCl (deposition time: 10 min) at T_{room}. Electrocatalyst layers with ternary coatings were called NiCuMo14, NiCuMo28, NiCuMo42 and NiCuMo56 depending on Mo ions concentration in the electrodeposition electrolyte.

2.2. Electrochemical measurements

Electrochemical measurements have been executed through a PARSTAT 2263. Any further treatments were carried out on as-prepared electrode obtained by electrodeposition. Geometric area of the electrodes was 2 cm^2. In these measurements, mercury/mercuric oxide/1 M NaOH electrode was used as reference. Electrode potential values were converted to Reversible Hydrogen Electrode (RHE) through the following expression:

$$E_{RHE} = E_{Hg/HgO} + 0.098\ V + 0.059\ pH \quad (1)$$

Double Layer capacitance was estimated by recording EIS spectra at 0.13 V RHE (frequency: 100 mHz–100 kHz, ac signal amplitude: 0.01 V) in neutral electrolyte (0.1 M ammonium biborate tetrahydrate aqueous solution, ABE, $(NH_4)_2B_4O_7 \times 4H_2O$, pH ∼ 9) in a N_2-saturated atmosphere.

To have information about the electrochemical performances, EIS spectra with the same settings were also carried out at −0.15 V RHE in 1 M KOH. Impedance spectra have been modelled through the software ZSimpWin using a proper equivalent electrical circuit (EEC), as reported below.

Linear sweep galvanodynamic measurements were performed at 0.001 A cm^{-2} s^{-1} between −0.001 and −0.1 A cm^{-2}, with 95% IR drop correction. The stability of the coatings was evaluated by galvanostatic measurements (0.1 A cm^{-2}, t = 100 h) but in a flow-through cell configuration with a flow rate of 420 mL min^{-1}. EIS spectra were recorded at −0.15 V RHE during the stability test at 25, 50, 75 and 100 h.

2.3. Morphological and structural characterization

Electrodes' morphology was studied by using a FEI Quanta 200 FEG SEM (Scanning Electron Microscope) (operating at 30 kV), joined to an X-ray energy dispersive system (EDX). A PanAnalytical Empyrean diffractometer with a Cu Kα anode (λ = 0.15405 nm) equipped with PIXCel1D detector was used to perform X-ray diffraction (XRD) measurements. The XRD patterns were collected over the 2θ angle range of 30°–80° using as operating conditions 40 kV and 40 mA.

Electrocatalysts surface composition was studied by X-ray Photoelectron Spectroscopy (XPS) analysis, carried out with a PHI 5000 VersaProbe II scanning microprobe (ULVAC-PHI), using a Al Kα source (1486.6 eV) and a X-ray beam of 100 μm diameter. A take-off angle of the emitted photoelectrons of 45° relative to the surface was used. Fitting procedure was carried out using MultiPak 9.9.0.8 software (ULVAC-PHI, Inc.), using Gauss-Lorentz model for peaks, an asymmetrical line shape for metallic species and a Shirley background.

2.4. Inductively Coupled Plasma-Optical Emission Spectroscopy

To estimate metal ions release to the testing solution during stability test, Inductively Coupled Plasma-Optical Emission Spectroscopy (ICP-OES) tests (PerkinElmer Inc.-Optima 2100 DV) were performed. A calibration with 0 (ultrapure water), 5, 10, 50, 100, 200, 500, 1000 ppb of Ni, Cu and Mo standard solution was carried out. Samplings were carried out at 25, 50, 75, 100 h.

3. Results and discussion

Ni substrate morphology is shown in Fig. 1.

Electrocatalyst layers for HER reaction were prepared by an electrodeposition route that allowed to deposit NiCuMo-based coatings on the surface of Ni substrates. Briefly, Ni, Cu and Mo are electrodeposited on the Ni substrate by applying a potential during the electrodeposition process (see experimental section) that is more cathodic than the equilibrium potential value for the reduction reaction of metal ions at pH = 2.5 [18,26]. The latter was set to 2.5 because working at higher pH can induce the precipitation of metal oxide/hydroxide at the electrode/electrolyte interface due to the low solubility products at high pH

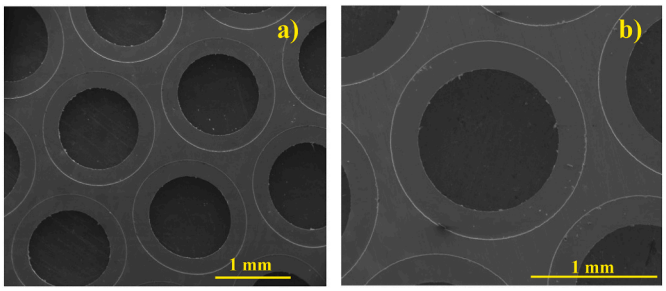

Fig. 1. SEM images of perforated plate type Ni electrode at different magnifications.

(see the Pourbaix diagrams for Ni, Cu and Mo [26]). Notably, under so strong cathodic polarization, hydrogen evolution can also occurs inducing a local pH increase on the electrode surface which can induce the deposition of the oxides due to electrogeneration of base. Setting pH = 2.5 and adding boric acid to the electrodeposition bath led to maintain acidic pH conditions at the electrode/electrolyte allowing the successful electrodeposition of metal species. To understand the effect of each metal on the catalyst activity, as well as any synergistic effect between Ni, Cu and Mo in improving HER performance, we synthesized coatings using pure metals (Ni, Cu, and Mo), binary mixtures (NiCu, NiMo, and CuMo), and ternary (NiCuMo) mixture. In the latter case (NiCuMo coating), several Mo molar concentrations in electrodeposition bath were investigated in order to maximize the electrocatalyst performance, i.e. to minimize the cathode overpotential at 100 mA cm^{-2} (η_{100}).

SEM images reported in Figs. S1–S3 show the morphologies of the coatings of pure metals, Ni, Cu and Mo, respectively. These SEM images demonstrated that the electrodeposition was successful. Moreover, EDX analyses confirmed the presence of Ni, Cu and Mo in the coating, depending on the electrodeposition bath composition. Notably, regardless of the coating composition, all the deposits were homogeneous throughout the whole substrate surface. Whilst Ni and Mo deposits are quite compact (see Figs. S1 and S3), Cu deposits have a higher roughness since the coating is formed by thin metallic needles (see Fig. S2). This indicates a significantly higher surface area of Cu coating with respect to Ni and Mo-based coatings. The influence of Cu increase on the ECSA can be also assessed by looking at the morphology of binary

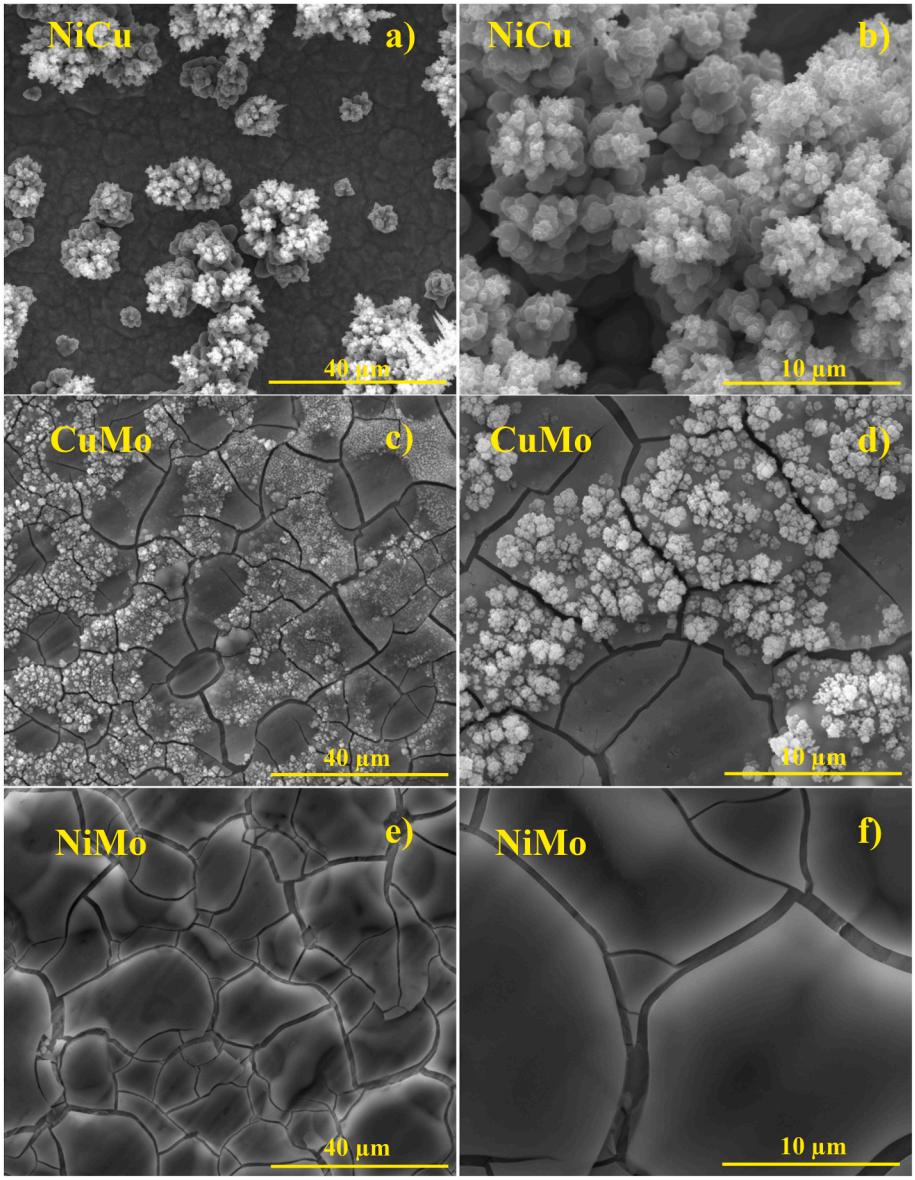

Fig. 2. Micrographs of NiCu coating on Ni substrate (a and b), of CuMo coating (c and d) and of NiMo coating (e and f) at different magnifications.

coatings. In fact, NiCu and CuMo electrodes' morphology is formed by clusters of nanoparticles (see Fig. 2a)-d)) even if the coatings deposited in these process conditions are not homogeneous (see Figs. S4 and S5).

The morphology of the NiMo coating is very similar to the morphology of the pure Mo coating (see Fig. S3) i.e. a compact deposit with lower surface area with respect to the other binary coatings. Morphologies of ternary coatings are shown in SEM images reported in Fig. 3 and Fig. S6 as a function of Mo molar concentration in electrodeposition bath. Regardless on Mo concentration, all the coatings are formed by particles, whose diameter depends on the composition of the electrodeposition bath, i.e. 1.1 ± 0.3 μm and 0.8 ± 0.25 μm for NiCuMo14 and NiCuMo42 coatings, respectively. High surface area is likely due to the presence of Cu, in agreement with the morphology of the pure Cu coating and all Cu-containing binary coatings.

To further confirm the successful electrodeposition of Ni, Cu, Mo, binary and ternary metallic mixtures, we also analyzed the samples using XRD, whose data are reported in Fig. 4.

All the samples, regardless on specific coating composition, are characterized by three main reflections related to the Ni substrate, i.e. $2\theta = 44.4°$, 51.3°, and 76.4°, matching (111), (200), and (220) planes, respectively, of face-centered cubic crystalline structure [18]. Adding Cu in the coating, mentioned reflections are shifted toward lower diffraction angle, since Cu atomic radius (1.278 Å) is higher than Ni atomic radius (1.245 Å) causing an expansion of Ni lattice [27,28]. The shoulder present at the base of (200) plane reflection is influenced from both Cu and Mo presence, as it is possible to note from the XRD patterns related to NiCu, NiMo and NiCuMo42 sample. To have a better picture of crystalline structure of investigated samples, we also carried out the electrodeposition processes on glass/FTO substrate [29] in the attempt to avoid recording the reflections coming from the Ni substrate and to have flat layers (see Fig. S7). Pure Ni coating is crystalline since Ni main reflections (see before) add to glass/FTO reflections. In the case of NiCu sample, shoulder peaks appear at the base of pure Ni sample (111) and (200) reflections, leading to the conclusion of a partial formation of NiCu alloy [30]. Addition effect of Mo in the coating is represented by the XRD pattern of NiCuMo42 sample electrodeposited on glass/FTO substrate. As it is possible to note, all the main reflections of pure Ni disappear, suggesting a highly disordered or poor crystalline structure. Moreover, no characteristic reflections of Mo or NiMo samples are detected, indicating that Mo atoms are probably dissolved into the lattice of Ni. A small and broad peak at ~43.5° was detected, which further

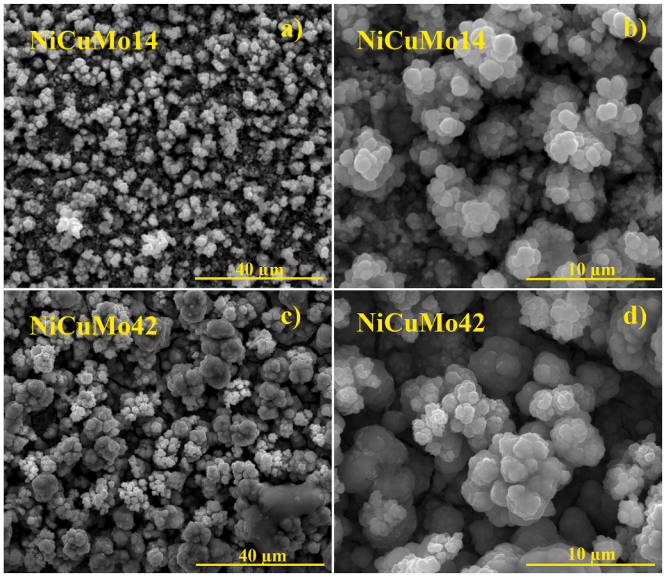

Fig. 3. SEM images of NiCuMo14 coating on Ni substrate (a and b) and of NiCuMo42 coating (c and d) at different magnifications.

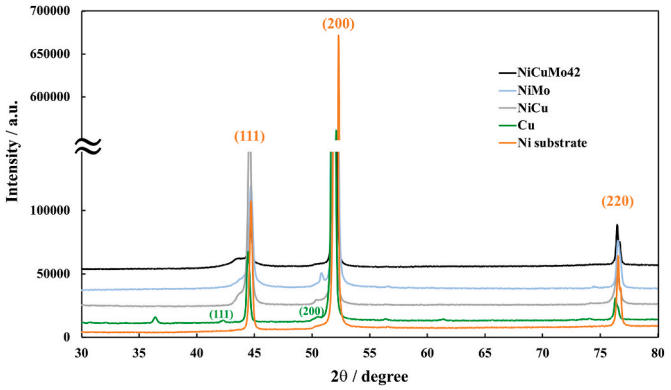

Fig. 4. XRD diffraction patterns of Ni substrate and several electrodeposited coatings (Cu, NiCu, NiMo and NiCuMo42).

suggests the poor crystallization of metallic Ni coating in spite Mo co-deposition.

Elemental composition of NiCu and of Mo-containing electrodes' surfaces was determined using XPS, whose survey scans are reported in Fig. 5a). XPS analysis of representative NiCuMo42 sample was shown where Ni 2p, Mo 3d and Cu 2p core level spectra are reported in Fig. 5b), c) and 5d), respectively.

Core level peak at 856.1 eV present in Ni 2p spectrum (see Fig. 5b)) is related to NiOOH species (i.e. Ni(III)) [31–33], probably derived from the oxidation of Ni contained in the coating due to air exposure. The formation of an oxyhydroxide could be also due to the local alkalinization of the environment close to the electrode surface during the electrodeposition due to hydrogen evolution. A small peak can be observed at 862.6 eV also due to the presence of NiOOH species [31–33]. In Fig. 5d) the Cu 2p core level spectrum exhibits a main peak at 932.2 eV, which is related to metallic Cu, and another two small peaks at 934.9 eV and 944.7 eV related to Cu(II) species [34–36]. Regarding Mo, as shown in Fig. 5c), two peaks are present, at 232.2 eV and 235.3 eV, both related to the oxidation of Mo to MoO_x. In Table 1 we reported the estimated surface composition of discussed samples.

The presence on the surface of oxidized species can be explained taking into account the formation of a thin passive layer on the samples [18]. Anyway, this phenomenon does not influence the activity of the electrodes (see below the electrochemical performances), since they work under cathodic polarization to activate HER, leading to the electrochemical reduction of the passive layer annulling the effect of air exposure on the samples.

3.1. Estimate of Electrochemical Active Surface Area

To further investigate the active area of the electrodeposited coatings, we estimated the Electrochemical Active Surface Area (ECSA), i.e. the electrode area that effectively contributes to the target reaction. ECSA estimate can be done by measuring electrodes' double layer capacitance, C_{dl}. For that, testing conditions were chosen to measure only non-Faradaic current, i.e. that related to the charging of double layer at electrode/electrolyte interface [37]. Subsequently, EIS spectra were recorded at 0.13 V RHE (−0.6 V SSC) electrode potential to thermodynamically avoid HER and also oxygen evolution reaction (OER), in an O_2-free environment to avoid the possible oxygen reduction reaction (ORR). EIS spectra for ternary coating are shown in Fig. 6a), and for Ni substrate, mono and binary coatings in Fig. S8. Furthermore, in Fig. 6b) equivalent electrical circuit used to fit the impedance data is reported. The circuit constitutes of a resistor R_{el} and a resistor R_{ct} in parallel with a constant phase element (CPE) Q_{dl}, where R_{el} represents the electrolyte resistance, R_{ct} the charge transfer resistance, and Q_{dl} the non-ideal double layer capacitance. Spectra fitting parameters are reported in Table 2.

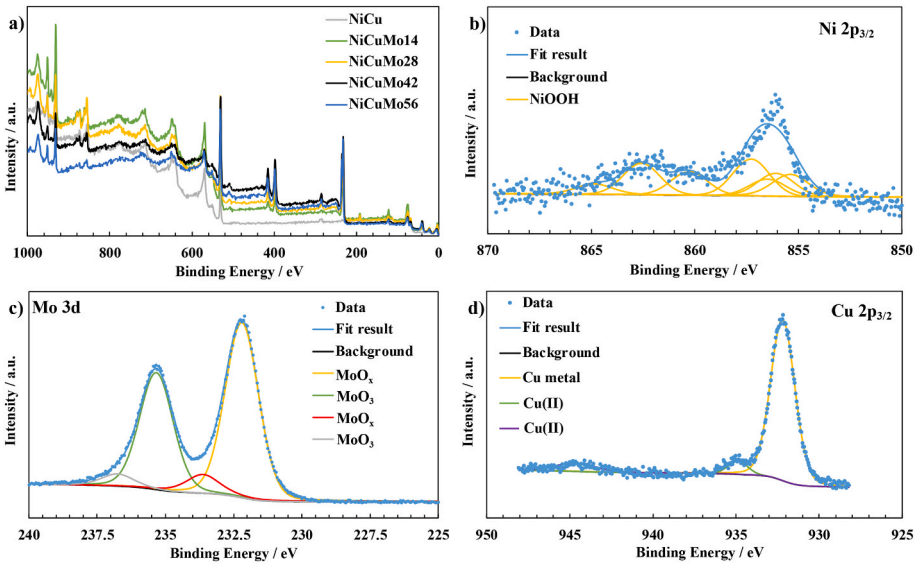

Fig. 5. a) XPS survey scans of NiCu and of Mo-containing samples. b) Ni 2p, c) Mo 3d and d) Cu 2p core level spectra of representative NiCuMo42 sample.

Table 1
Elemental composition of NiCu and of Mo-containing samples estimated by XPS. Balance at.% is related to adventitious carbon.

Sample	O [at%]	Ni [at%]	Cu [at%]	Mo [at%]
NiCu	48.3	15.4	21.6	–
NiCuMo14	67.1	8.8	15.2	5.3
NiCuMo28	64.6	11.5	6.0	7.0
NiCuMo42	58.0	5.9	5.0	13.7
NiCuMo56	62.3	2.8	6.4	14.1

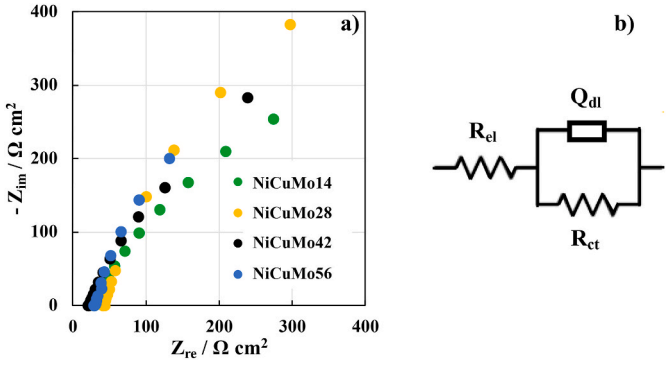

Fig. 6. a) Nyquist plot of the EIS spectra recorded at 0.13 V RHE in 0.1 M ABE. b) Electrical circuit used for modelling and fitting EIS spectra.

Table 2
Fitting parameters of EIS spectra recorded at 0.13 V RHE in 0.1 M ABE related to all the ternary coating electrodes.

Sample	R_{el} [Ω cm^2]	Q_{dl} [S s^n cm^{-2}]	n	R_{ct} [Ω cm^2]
NiCuMo14	30	2.9 10^{-3}	0.71	970
NiCuMo28	40	2.8 10^{-3}	0.81	1060
NiCuMo42	22	4.6 10^{-3}	0.77	900
NiCuMo56	30	6.2 10^{-3}	0.82	1040

It can be noted that R_{ct} is, in any case, higher than 900 Ω cm^2, as expected in these operating conditions, showing the behaviour of an ideally polarizable interface. To estimate the effective double layer capacitance from the CPE value, we used the following relationship [38]:

$$C_{dl} = {Q_{dl}}^{1/n} {R_{el}}^{(1-n)/n} \quad (2)$$

By knowing electrodes' C_{dl} values, it is possible to estimate the roughness factor, r, as an indication of the ECSA by the following relationship:

$$r = \frac{C_{dl}}{40\ \mu F\ cm^{-2}} \quad (3)$$

considering as reference value 40 μF cm^{-2}, that is the double layer capacitance value we measured for a flat mirror-finished Ni sample. All the roughness factors estimated for initial Ni substrate and for ternary coatings are reported in Table 3, whilst those estimated for the other coatings are reported in Table S2.

The pristine Ni substrate has r = 0.8 due to the presence of holes whilst electrodeposited electrodes have a higher r, with NiCuMo56 electrode showing more than a 100-fold increase in ECSA with respect to initial substrate. This result is in agreement with information collected by SEM images, i.e. a higher surface area of ternary coating electrodes due to the formation of particles clusters during the electrodeposition process. It is noteworthy to mention that a higher ECSA is beneficial for an improvement in HER performance, increasing the activity of the electrodes [39–41].

3.2. *Evaluation of the electrocatalytic performance of the electrodes*

Electrocatalytic performance of electrodeposited NiCuMo on Ni substrate toward HER in alkaline environment (1 M KOH) was studied by galvanodynamic measurements and by recording EIS spectra. For these measurements, a typical three-electrode setup was used where NiCuMo electrode was the working electrode. Regardless on reference electrode used for the electrochemical characterization, all the electrode potential values are referred to RHE (see eq. (1)). Fig. 7a) shows current density vs electrode potential curves recorded with bare Ni substrate, NiCu electrode and all the electrodes with ternary coatings, corrected with 95% IR drop.

Ni substrate reported worst performance in terms of overpotential needed for the activation of HER. In fact, to reach a current density value of 10 mA cm^{-2} and 100 mA cm^{-2}, 330 mV and 480 mV are needed, respectively. Better performances were reached with the addition of Cu, leading to cathodic overpotential of $\eta_{10} = 280$ mV and $\eta_{100} = 390$ mV (at corresponding current densities of 10 mA cm^{-2} and 100 mA cm^{-2},

Table 3
Roughness factor of Ni substrate and all the electrodes with ternary coatings produced by electrodeposition process on Ni substrate.

	Ni substrate	NiCuMo14 electrode	NiCuMo28 electrode	NiCuMo42 electrode	NiCuMo56 electrode
Roughness factor r	0.8	27	42	57	105

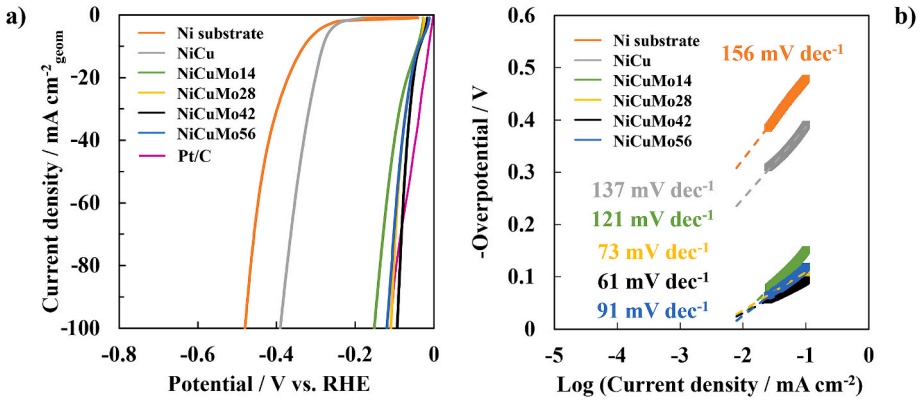

Fig. 7. a) Polarization curves recorded in 1 M KOH for several electrodes with 95% IR drop correction (including pristine Ni substrate). b) Tafel plot with corresponding slope values. Benchmark: Pt/C [29].

respectively). The addition of Mo further enhances HER performance. In particular, as shown in Fig. 7a), best performance is reached with NiCuMo42 electrode, especially at high current densities, with a η_{100} = 95 mV. The cathodic overpotential at 10 mA cm^{-2} (η_{10} = 36 mV) is similar or lower [42] than values previously reported in the literature for HER electrocatalysts in alkaline solutions. Moreover, η_{10} and η_{100} values are lower with respect to other Ni-based electrocatalysts (e.g. Ni phosphides, Ni chalcogenides, Ni nitrides, Ni carbides and Ni borides), produced through different synthesis ways, tested in alkaline environment [12]. All η_{10} and η_{100} values estimated with galvanodynamic measurements are reported in Table 4.

Mono and binary electrocatalysts showed worse overall performances than ternary (Mo-containing) electrodes, as reported in Fig. S9.

Fig. 7b shows Tafel plots (η vs log(i) plot) derived from polarization curves reported in Fig. 7a. Slope of Tafel line is an important kinetic parameter since it is related to the reaction mechanism, identifying what is the rate determining step of the overall mechanism. The HER reaction can be written in two steps.

First step:

$$H2O + M + e- \leftrightarrow M - H* + OH- \qquad b = 29\ mV\ dec^{-1} \qquad (4)$$

Second step:

$$H2O + M - H* + e- \leftrightarrow H2 + M + OH- \qquad b = 39\ mV\ dec^{-1} \qquad (5)$$

$$2M - H* \leftrightarrow 2M + H2 \qquad b = 116\ mV\ dec^{-1} \qquad (6)$$

Depending on the Tafel slope, Volmer step (hydrogen adsorption, see eq. (4)), Heyrovsky step (electrochemical hydrogen desorption, see eq. (5)) or Tafel step (reaction of two adsorbed hydrogen atoms, see eq. (6)) can be identified as rate determining step [43]. Moreover, the lower the Tafel slope, the lower is the overpotential needed to deliver a certain current density value, i.e. the electrocatalytic activity of the electrode is increased. Tafel slope of Ni substrate is 156 mV dec^{-1} whilst the lowest Tafel slope value is reported for the reaction carried out with NiCuMo42 electrode, namely 61 mV dec^{-1}. Notably, Mo and NiMo-based electrodes showed low Tafel slopes (63 and 69 mV dec^{-1}, see Fig. S9) demonstrating the beneficial effect of Mo in improving HER performance, even though these electrodes have higher onset overpotential values, therefore η_{10} and η_{100} values. It is noteworthy to mention that the increase in electrochemical performance of Mo-based electrodes is also surely related to the higher estimated ECSA with respect to that estimated for bare Ni substrate, highlighting the synergistical effect of composition and morphology in obtaining highly active electrodes.

Table 4
η_{10} and η_{100} values of Ni substrate, NiCu and all the electrodes with ternary coatings produced by electrodeposition process on Ni substrate.

Sample	η_{10} [mV]	η_{100} [mV]
Ni substrate	330	480
NiCu	280	390
NiCuMo14	43	150
NiCuMo28	35	110
NiCuMo42	36	95
NiCuMo56	38	120

To gain more insight about HER kinetics, we also recorded EIS spectra at −0.15 V RHE to have information about the charge transfer resistance. EIS spectra are reported in Fig. 8 in Nyquist representation, and they were modelled and fitted considering the electrical circuit reported in Fig. 6b).

Lowest R_{ct} was estimated for NiCuMo42 electrode (0.4 Ω cm^2), in agreement with what observed from polarization curves shown in Fig. 7a), whilst the highest R_{ct} (the lowest electrocatalytic activity) was estimated for perforated plate type Ni electrode, i.e. 600 Ω cm^2 (see Fig. S10). Therefore, our strategy to maximize electrochemical performance of the electrodes for HER was synthesizing Ni-based electrode and, at the same time, increasing ECSA by adding Cu to the coating and optimizing Mo content to maximize the intrinsic electrocatalytic activity. This is also in agreement with the Brewer-Engel valence-bond theory, i.e. metals having empty or half-filled d-orbitals (e.g. Mo) alloyed with metals (e.g. Ni) having internally paired d-electrons (which would not be available for bonding) have electrocatalytic activity toward HER higher than single metal electrocatalytic activity [44]. Moreover, Cu shows weak M − H bond whilst Mo shows strong M − H bond, allowing a good compromise with an improvement of electrocatalytic activity.

3.3. Investigation of coating stability via long-run tests

Besides the electrocatalytic activity, another crucial parameter to have efficient electrodes is the stability of the coating. To test the long-term stability of the best performing electrode (NiCuMo42), we carried out galvanostatic measurements at 0.1 A cm^{-2} for 100 h in 1 M KOH

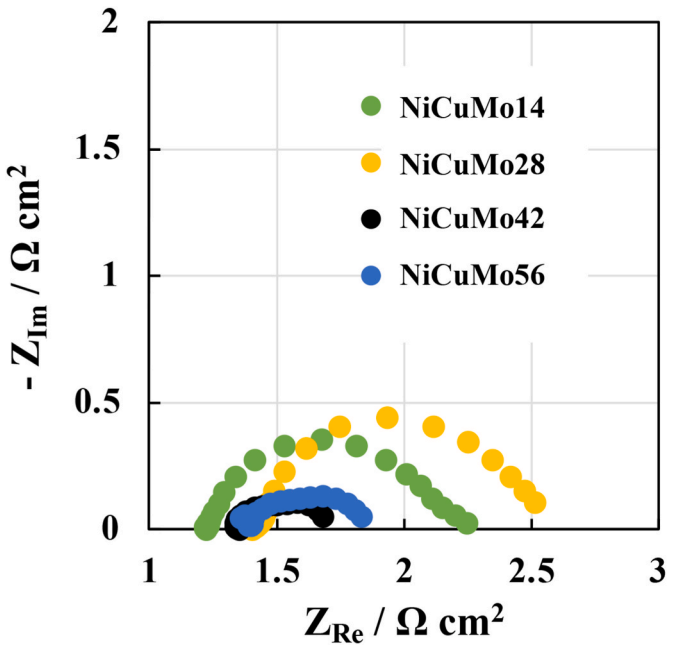

Fig. 8. Nyquist plot of EIS spectra recorded at −0.15 V RHE for the ternary coating electrodes.

electrolyte. Resulting electrode potential vs time curve is shown in Fig. 9a.

We carried out stability test in a flow cell to mimic industrial electrolyzers which have defined flow conditions, and consequently to check the adhesion of our catalyst layer when it is exposed to an electrolyte flow. For optimized bubble management, we opted for a flow-through electrolyte flow configuration where the electrolyte flow path goes through the electrode (from its back side to its front side), thus flushing the produced gas bubbles from the electrode. After an initial increase in overpotential (first 20 h), no significant degradation in electrocatalytic performance was observed, proving the good stability of the electrode. To further study the stability of the electrode, we also recorded EIS spectra at −0.15 V RHE every 25 h of stability test, that are shown in Fig. 9b). Impedance spectra fitting parameters are reported in Table 5.

Notably, with time there was a decrease of the double layer capacitance (considering that the n exponent of the CPE element is almost constant with time) and an increase in R_{ct} value. These two parameters can be considered as the result of a decrease in ECSA during the stability test. This effect can be also assessed from the SEM image reported in Fig. 10 where electrode morphology after long-term stability test is shown. Although electrocatalyst layer morphology changed, such change did not significantly compromise the electrocatalytic activity of the electrode.

Regarding electrode stability, it is important to understand if during operating and shutdown conditions of the electrolyser some of the metallic components of electrocatalytic layer could be lost by dissolution. To this aim, we analyzed samples of the solution where we carried out stability test by ICP-OES. Whilst Ni and Cu content in the solution were totally negligible, Mo content was detected proving a slow dissolution rate, with a maximum content of Mo equal to 2.1 ppm and a release rate of 0.0435 mg cm^{-2} h^{-1}, also proving the high durability of the electrode.

Table 5
Fitting parameters of EIS spectra recorded at −0.15 V RHE in 1 M KOH related to NiCuMo42 electrode at different times of stability test.

Time [h]	R_{el} [Ω cm^2]	Q_{dl} [S s^n cm^{-2}]	n	R_{ct} [Ω cm^2]
25	1.4	4.2 10^{-2}	0.72	4.95
50	1.7	4.0 10^{-2}	0.76	6.51
75	1.7	3.4 10^{-2}	0.73	6.80
100	1.9	3.1 10^{-2}	0.72	8.35

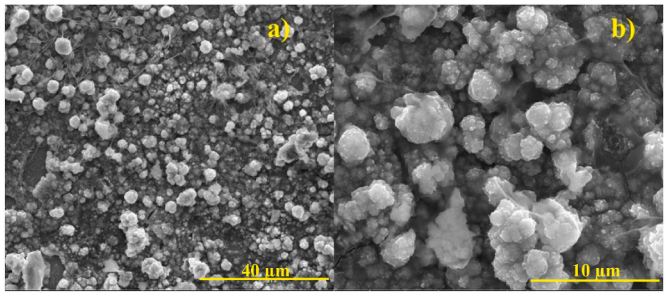

Fig. 10. SEM images of NiCuMo42 electrode after 100 h of stability test at different magnifications (a and b).

4. Conclusions

In this work, functionalized Ni-based electrodes to be used as cathodes in alkaline electrolyzers were prepared and characterized. Catalyst layers were composed of Ni, Cu and Mo-based coatings prepared by a one step electrodeposition process, easily scalable at the industrial level. The effect of every single coating component on the ECSA and on the catalytic activity of the electrodes was evaluated by electrochemical investigation and imaging. Our results showed NiCuMo42 to be the best of the tested catalyst compositions, having a cathodic overpotential of 36 mV at 10 mA cm^{-2}, and 95 mV at 100 mA cm^{-2} which is one of the lowest overpotential values reported in literature for PGM-free electrodes for HER.

The electrode sustained its electrocatalytic performance throughout a 100 h long durability test, even if with a slight increase in overpotential value, including a good chemical stability since Ni and Cu content in the electrolyte after the test were negligible, whilst Mo dissolution was detected but with a low rate. Notably, our tests were carried out with the electrolyte flowing through the electrode, further proving the good adhesion and stability of the coating.

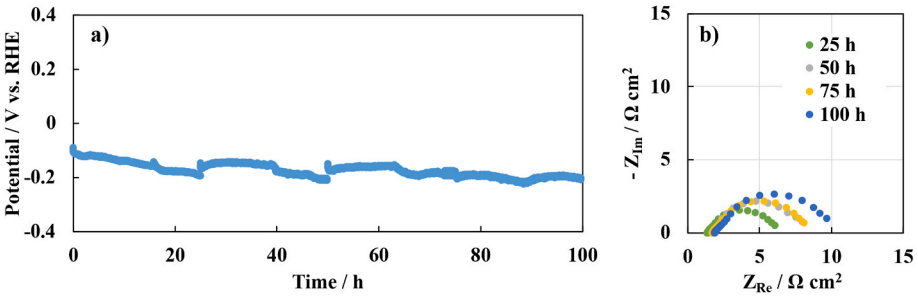

Fig. 9. a) Potential vs time curve related to stability test at 0.1 A cm^{-2}. b) EIS spectra recorded after every 25 h during stability test.

An optimized catalyst layer led to very high performances, combining the presence of PGM-free elements with a high electrochemical activity, which are crucial characteristics for next-generation zero-gap alkaline electrolyzers. Future works should be focused on further optimization of Ni substrate geometry, electrocatalyst composition and on the accelerated stress testing under industrially-relevant conditions.

CRediT authorship contribution statement

Francesco Di Franco: Conceptualization, Methodology, Supervision, Visualization, Writing – review & editing. **Andrea Zaffora:** Conceptualization, Data curation, Formal analysis, Methodology, Supervision, Visualization, Writing – original draft, Writing – review & editing. **Davide Pupillo:** Data curation, Formal analysis, Investigation, Writing – review & editing. **Barbara Seminara:** Data curation, Investigation. **Ragne Pärnamäe:** Data curation, Formal analysis, Supervision, Writing – review & editing. **Michele Tedesco:** Formal analysis, Supervision, Writing – review & editing. **Monica Santamaria:** Conceptualization, Formal analysis, Funding acquisition, Resources, Supervision, Visualization, Writing – review & editing.

Declaration of competing interest

The authors declare that they have no known competing financial interests or personal relationships that could have appeared to influence the work reported in this paper.

Acknowledgements

Veco Precision BV (The Netherlands) is gratefully acknowledged for providing Ni electrodes.

The work of R.P. and M.T. was performed in the cooperation framework of Wetsus, European Centre of Excellence for Sustainable Water Technology. Wetsus is co-funded by the Dutch Ministry of Economic Affairs and Ministry of Infrastructure and Environment, the Province of Fryslân, and the Northern Netherlands Provinces (www.wetsus.eu). Advanced Technologies Network (ATeN) Center (University of Palermo) is also acknowledged for XPS measurements.

Appendix A. Supplementary data

Supplementary data to this article can be found online at https://doi.org/10.1016/j.ijhydene.2024.05.164.

References

[1] Zhang L, Jia C, Bai F, Wang W, An S, Zhao K, et al. A comprehensive review of the promising clean energy carrier: hydrogen production, transportation, storage, and utilization (HPTSU) technologies. Fuel 2024;355. https://doi.org/10.1016/j.fuel.2023.129455.

[2] AlHumaidan FS, Absi Halabi M, Rana MS, Vinoba M. Blue hydrogen: current status and future technologies. Energy Convers Manag 2023;283. https://doi.org/10.1016/j.enconman.2023.116840.

[3] Le TT, Sharma P, Bora BJ, Tran VD, Truong TH, Le HC, et al. Fueling the future: a comprehensive review of hydrogen energy systems and their challenges. Int J Hydrogen Energy 2024;54:791–816. https://doi.org/10.1016/j.ijhydene.2023.08.044.

[4] Hosseini SE, Wahid MA. Hydrogen production from renewable and sustainable energy resources: promising green energy carrier for clean development. Renew Sustain Energy Rev 2016;57:850–66. https://doi.org/10.1016/j.rser.2015.12.112.

[5] Qi J, Zhang W, Cao R. Solar-to-Hydrogen energy conversion based on water splitting. Adv Energy Mater 2018;8. https://doi.org/10.1002/aenm.201701620.

[6] Ishaq H, Dincer I, Crawford C. A review on hydrogen production and utilization: challenges and opportunities. Int J Hydrogen Energy 2022;47:26238–64. https://doi.org/10.1016/j.ijhydene.2021.11.149.

[7] Zhang W, Liu M, Gu X, Shi Y, Deng Z, Cai N. Water electrolysis toward elevated temperature: advances, challenges and frontiers. Chem Rev 2023;123:7119–92. https://doi.org/10.1021/acs.chemrev.2c00573.

[8] Raveendran A, Chandran M, Dhanusuraman R. A comprehensive review on the electrochemical parameters and recent material development of electrochemical water splitting electrocatalysts. RSC Adv 2023;13:3843–76. https://doi.org/10.1039/d2ra07642j.

[9] International Renewable Energy Agency (IRENA). Green hydrogen cost reduction: scaling up electrolysers to meet the 1.5°C climate goal, XX, abu dhabi. 2020.

[10] Gong M, Wang DY, Chen CC, Hwang BJ, Dai H. A mini review on nickel-based electrocatalysts for alkaline hydrogen evolution reaction. Nano Res 2016;9:28–46. https://doi.org/10.1007/s12274-015-0965-x.

[11] Krishnan A, Ajith A, Krishnan AV, Saji RE, Syamli S, Shibli SMA. Ni-Based electro/photo-catalysts in HER – a review. Surface Interfac 2023;36. https://doi.org/10.1016/j.surfin.2022.102619.

[12] Hu C, Lv C, Zeng N, Liu A, Liu Y, Hu L, et al. Recent advances in Ni-based electrocatalysts for hydrogen evolution reaction. Energy Technol 2023;11. https://doi.org/10.1002/ente.202201048.

[13] Guo J, Wang B, Yang D, Wan Z, Yan P, Tian J, et al. Rugae-like Ni2P-CoP nanoarrays as a bi-functional catalyst for hydrogen generation: NaBH4 hydrolysis and water reduction. Appl Catal, B 2020;265. https://doi.org/10.1016/j.apcatb.2019.118584.

[14] McKay IS, Schwalbe JA, Goodman ED, Willis JJ, Majumdar A, Cargnello M. Elucidating the synergistic mechanism of nickel-molybdenum electrocatalysts for the hydrogen evolution reaction. MRS Commun 2016;6:241–6. https://doi.org/10.1557/mrc.2016.27.

[15] Luo M, Yang J, Li X, Eguchi M, Yamauchi Y, Wang ZL. Insights into alloy/oxide or hydroxide interfaces in Ni-Mo-based electrocatalysts for hydrogen evolution under alkaline conditions. Chem Sci 2023;14:3400–14. https://doi.org/10.1039/d2sc06298d.

[16] Bau JA, Kozlov SM, Azofra LM, Ould-Chikh S, Emwas AH, Idriss H, et al. Role of oxidized Mo species on the active surface of Ni-Mo electrocatalysts for hydrogen evolution under alkaline conditions. ACS Catal 2020;10:12858–66. https://doi.org/10.1021/acscatal.0c02743.

[17] Bao F, Kemppainen E, Dorbandt I, Bors R, Xi F, Schlatmann R, et al. Understanding the hydrogen evolution reaction kinetics of electrodeposited nickel-molybdenum in acidic, near-neutral, and alkaline conditions. Chemelectrochem 2021;8:195–208. https://doi.org/10.1002/celc.202001436.

[18] Zaffora A, Di Franco F, Pupillo D, Seminara B, Tranchida G, Santamaria M. Highly active and stable NiCuMo electrocatalyst supported on 304 stainless steel porous transport layer for hydrogen evolution in alkaline water electrolyzer. Adv Sustain Syst 2023;7. https://doi.org/10.1002/adsu.202200486.

[19] Santos HLS, Corradini PG, Medina M, Dias JA, Mascaro LH. NiMo-NiCu inexpensive composite with high activity for hydrogen evolution reaction. ACS Appl Mater Interfaces 2020;12:17492–501. https://doi.org/10.1021/acsami.0c00262.

[20] Zhang J, Lu H, He P, Ren Z, Shen G, Liu R, et al. The performance and corrosion resistance of an electrodeposited Ni-Mo-Cu HER catalyst. Surf Coat Technol 2023;465. https://doi.org/10.1016/j.surfcoat.2023.129596.

[21] Xia M, Lei T, Lv N, Li N. Synthesis and electrocatalytic hydrogen evolution performance of Ni-Mo-Cu alloy coating electrode. Int J Hydrogen Energy 2014;39:4794–802. https://doi.org/10.1016/j.ijhydene.2014.01.091.

[22] Angulo A, van der Linde P, Gardeniers H, Modestino M, Fernández Rivas D. Influence of bubbles on the energy conversion efficiency of electrochemical reactors. Joule 2020;4:555–79. https://doi.org/10.1016/j.joule.2020.01.005.

[23] Yuan S, Zhao C, Cai X, An L, Shen S, Yan X, et al. Bubble evolution and transport in PEM water electrolysis: mechanism, impact, and management. Prog Energy Combust Sci 2023;96. https://doi.org/10.1016/j.pecs.2023.101075.

[24] Rocha F, Delmelle R, Georgiadis C, Proost J. Effect of pore size and electrolyte flow rate on the bubble removal efficiency of 3D pure Ni foam electrodes during alkaline water electrolysis. J Environ Chem Eng 2022;10. https://doi.org/10.1016/j.jece.2022.107648.

[25] Sun H, Xu X, Kim H, Jung WC, Zhou W, Shao Z. Electrochemical water splitting: bridging the gaps between fundamental research and industrial applications. Energy and Environmental Materials 2023;6. https://doi.org/10.1002/eem2.12441.

[26] Pourbaix M. Atlas of electrochemical equilibria in-aqueous solutions. n.d...

[27] Teng X, Wang J, Ji L, Liu Y, Zhang C, Chen Z. Fabrication of three-dimensional multiscale porous alloy foams at a planar substrate for efficient water splitting. ACS Sustainable Chem Eng 2019;7:5412–9. https://doi.org/10.1021/acssuschemeng.8b06452.

[28] Wang K, Xia M, Xiao T, Lei T, Yan W. Metallurgically prepared NiCu alloys as cathode materials for hydrogen evolution reaction. Mater Chem Phys 2017;186:61–6. https://doi.org/10.1016/j.matchemphys.2016.10.029.

[29] Li Y, Tan X, Hocking RK, Bo X, Ren H, Johannessen B, et al. Implanting Ni-O-VOx sites into Cu-doped Ni for low-overpotential alkaline hydrogen evolution. Nat Commun 2020;11. https://doi.org/10.1038/s41467-020-16554-5.

[30] Kumar M, Shetti NP. Magnetron sputter deposited NiCu alloy catalysts for production of hydrogen through electrolysis in alkaline water. Mater Sci Energy Technol 2018;1:160–5. https://doi.org/10.1016/j.mset.2018.06.010.

[31] Grosvenor AP, Biesinger MC, Smart RSC, McIntyre NS. New interpretations of XPS spectra of nickel metal and oxides. Surf Sci 2006;600:1771–9. https://doi.org/10.1016/j.susc.2006.01.041.

[32] Biesinger MC, Payne BP, Grosvenor AP, Lau LWM, Gerson AR, Smart RSC. Resolving surface chemical states in XPS analysis of first row transition metals, oxides and hydroxides: Cr, Mn, Fe, Co and Ni. Appl Surf Sci 2011;257:2717–30. https://doi.org/10.1016/j.apsusc.2010.10.051.

[33] Biesinger MC, Payne BP, Lau LWM, Gerson A, Smart RSC. X-ray photoelectron spectroscopic chemical state Quantification of mixed nickel metal, oxide and hydroxide systems. Surf Interface Anal 2009;41:324–32. https://doi.org/10.1002/sia.3026.

[34] Cornette P, Zanna S, Seyeux A, Costa D, Marcus P. The native oxide film on a model aluminium-copper alloy studied by XPS and ToF-SIMS. Corrosion Sci 2020;174. https://doi.org/10.1016/j.corsci.2020.108837.
[35] Kim A, Muthuchamy N, Yoon C, Joo SH, Park KH. MOF-derived cu@cu2O nanocatalyst for oxygen reduction reaction and cycloaddition reaction. Nanomaterials 2018;8. https://doi.org/10.3390/nano8030138.
[36] Kautek W, Gordon JG. XPS studies of anodic surface films on copper electrodes. J Electrochem Soc 1990;137:2672. https://doi.org/10.1149/1.2087008.
[37] Bard AJ, Faulkner LR. Electrochemical methods: fundamentals and applications. second ed. John Wiley & Sons; 2001.
[38] Hirschorn B, Orazem ME, Tribollet B, Vivier V, Frateur I, Musiani M. Determination of effective capacitance and film thickness from constant-phase-element parameters. Electrochim Acta 2010;55:6218–27. https://doi.org/10.1016/j.electacta.2009.10.065.
[39] Xu L, Li W, Luo J, Chen L, He K, Ma D, et al. Carbon-based materials as highly efficient catalysts for the hydrogen evolution reaction in microbial electrolysis cells: mechanisms, methods, and perspectives. Chem Eng J 2023;471. https://doi.org/10.1016/j.cej.2023.144670.
[40] Anantharaj S, Noda S. Electrochemical dealloying-assisted activity enhancement: the next big thing in water electrosplitting. Nano Energy 2023;114. https://doi.org/10.1016/j.nanoen.2023.108624.
[41] Nazari M, Ghaemmaghami M. Approach to evaluation of electrocatalytic water splitting parameters, reflecting intrinsic activity: toward the right pathway. ChemSusChem 2023;16. https://doi.org/10.1002/cssc.202202126.
[42] Dong S, Li Y, Zhao Z, Li R, He J, Yin J, et al. A review of the application of heterostructure catalysts in hydrogen evolution reaction. ChemistrySelect 2022;7. https://doi.org/10.1002/slct.202104041.
[43] Zhu J, Hu L, Zhao P, Lee LYS, Wong KY. Recent advances in electrocatalytic hydrogen evolution using nanoparticles. Chem Rev 2020;120:851–918. https://doi.org/10.1021/acs.chemrev.9b00248.
[44] Jaksic MM. Advances in electrocatalysis for hydrogen evolution in the light of the brewer-engel valence-bond theory. Int J Hydrogen Energy 1987;12:727–52.